The Astrophysical Journal, 925:209 (8pp), 2022 February 1 https://doi.org/10.3847/1538-4357/ac423a

The Neutron Energy Spectra of Lunar Meteorites Evaluated from Sm and Er Isotopic Compositions

Hiroshi Hidaka[1], Shigekazu Yoneda[2], Kunihiko Nishiizumi[3], and Marc Caffee[4]
[1] Department of Earth and Planetary Science, Nagoya University, Nagoya 464-8601, Japan; hidaka@eps.nagoya-u.ac.jp
[2] Department of Science and Engineering, National Museum of Nature and Science, Tsukuba 305-0005, Japan
[3] Space Science Laboratory, University of California, Berkeley, CA 94720-7450, USA
[4] Department of Physics and Astronomy, Purdue University, IN 47907-2036, USA
Received 2021 September 13; revised 2021 December 3; accepted 2021 December 9; published 2022 February 7

Abstract

Cosmic-ray exposure records of 13 lunar meteorites, Dhofar 081, Dhofar 910, Dhofar 911, Northwest Africa (NWA) 482, NWA 2995, NWA 2996, NWA 3136, NWA 3163, NWA 4472, NWA 4734, NWA 4884, NWA 4932, and NWA 4936, were characterized from the abundances of spallogenic (^{10}Be and ^{26}Al) and neutron-captured (^{36}Cl, ^{41}Ca,^{150}Sm, and ^{168}Er) nuclides produced by cosmic-ray irradiation. Assuming a single-stage irradiation model for individual meteorites, 11 of the 13 meteorites had resided at shallow depths in the range of 55 to 330 g cm^{-2} from the lunar surface and experienced cosmic-ray irradiations for 140–870 Ma on the Moon. In contrast, 2 of the 13 meteorites, Dhofar 911 and NWA 4932, cannot be simply explained by a single-stage irradiation, but need at least two-stage irradiation on the Moon. Furthermore, the neutron fluences of thermal and epithermal energy regions for individual meteorites were quantified from a combination of the isotopic shifts of ^{149}Sm–^{150}Sm and ^{167}Er–^{168}Er, respectively. Our estimates gave 8–11 times higher epithermal neutron fluences (1.7–13.7 $\times$ 10^{17} neutrons cm^{-2}) than the thermal neutron fluences (0.65–13.8 $\times$ 10^{16} neutrons cm^{-2}) for 9 of the 13 meteorites, which are consistent with those from the lunar regolith materials in our previous study. This result also supports the long cosmic-ray irradiation of most lunar meteorites on the surface of the Moon.

Unified Astronomy Thesaurus concepts: Galactic cosmic rays (567); Lunar surface (974); Isotope shifts (2069)

1. Introduction

As a result of the interaction between cosmic rays and planetary materials without atmospheric layers in space, two types of nuclear reactions, spallation and neutron capture, mainly occur at the surficial parts of the materials. The products from such nuclear reactions, what we call cosmogenic nuclides, can be used to understand the surface evolution process of the planetary material. Cosmogenic nuclides like ^{10}Be (half-life = 1.5 Ma), ^{26}Al (half-life = 0.71 Ma) and ^{53}Mn (half-life = 3.7 Ma) are produced by spallation reactions, and ^{36}Cl (half-life = 0.30 Ma), ^{41}Ca (half-life = 0.10 Ma), ^{150}Sm (stable) and ^{158}Gd (stable) are by neutron-capture reactions. Because the quantities and production rates of individual cosmogenic nuclides vary with the depth from the surface of the target materials in the original body and their chemical compositions, a comparison of the abundances of multiple cosmogenic nuclides detected from the same single fragment of meteorites and lunar surficial materials provides useful information to characterize the cosmic-ray exposure (CRE) histories.

Among the cosmogenic nuclides produced by cosmic-ray interactions, short-lived radionuclides (SLRs) such as ^{10}Be, ^{26}Al, ^{36}Cl, ^{41}Ca, and ^{53}Mn have been detected using accelerator mass spectrometry (AMS) as one of the most sensitive analytical methods (e.g., Imamura et al. 1973; Nishiizumi et al. 1984a, 1984b, 1997). The production rates of the cosmogenic radionuclides largely depend upon the size of a small target material in space exposure (4π exposure) conditions and upon the depth in a large target object in surface exposure (2π exposure) conditions. Here, 4π refers to space exposure, whereas 2π is exposure on the surface of a large body. The comparison of the concentrations of the cosmogenic radionuclides with calculated production rates from the conventional models can constrain the exposure history of a meteorite like the estimation of the preatmospheric size of meteoroid, depth of meteorite in the parent body, and transition time from the parent body to the Earth (e.g., Honda et al. 2002; Welten et al. 2003, 2011).

While the SLRs provide the CRE information for the recent few million years in association with their half-lives, the neutron-captured isotopic shifts of ^{149}Sm–^{150}Sm and ^{157}Gd–^{158}Gd reflect the accumulation of the CRE records since the formation of the planetary materials. Because some isotopes of rare earth elements (REEs), such as ^{149}Sm and ^{157}Gd, are sensitive to reaction with thermal neutrons ($E < 0.1$ eV), the variations of isotopic abundances of ^{149}Sm,^{150}Sm, ^{157}Gd, and ^{158}Gd by the neutron-capture reactions of ^{149}Sm(n,γ)^{150}Sm and ^{157}Gd(n,γ)^{158}Gd, respectively, have often been found in meteorites (Hidaka et al. 1999, 2000a). The thermal neutron fluence, Ψ_{th}, the total amount of thermalized neutrons produced in association with the cosmic-ray irradiations, can be estimated quantitatively from the isotopic shifts of ^{149}Sm–^{150}Sm and ^{157}Gd–^{158}Gd. In addition, the isotopic shift of ^{167}Er–^{168}Er has been used effectively to quantify a part of the epithermal (0.1 eV $< E <$ 500 keV) neutron fluence Ψ_{epi}, because ^{167}Er has a high resonance integral (RI) in the epithermal neutron energy region (0.1 eV $< E <$ 2000 eV). Considering that the neutron energy spectrum in the range from thermal to epithermal regions sensitively varies with the presence of hydrogen and carbon, the ratio of neutron fluences Ψ_{epi}/Ψ_{th} estimated from the combination of the neutron-captured isotopic data of Sm,

Table 1
Abundances of Cosmogenic Radionuclides (dpm kg^{-1}) and Estimated Burial Depth on the Moon

Sample	Depth from Sample Surface	^{10}Be	^{26}Al	^{36}Cl	^{41}Ca	Burial Depth (g cm^{-2})
Dhofar 081	exterior	5.38 ± 0.10	31.2 ± 0.8	7.16 ± 0.11	201 ± 18	200–230
	interior	5.18 ± 0.09	31.9 ± 0.9	7.40 ± 0.12	215 ± 13	
Dhofar 910		5.36 ± 0.05	34.6 ± 0.9	8.39 ± 0.12	189 ± 7	>1100
Dhofar 911		0.045 ± 0.011	0.334 ± 0.072	0.10 ± 0.01	2.57 ± 0.99	>1100
NWA 2996		5.04 ± 0.12	32.0 ± 1.6	7.27 ± 0.21		230
NWA 3136		9.44 ± 0.20	49.6 ± 1.7	10.1 ± 0.31		30–80
NWA 3163	0–2 mm	3.07 ± 0.09	20.6 ± 0.9	6.08 ± 0.19		320
	0–1 mm	3.00 ± 0.12	18.0 ± 0.6	5.90 ± 0.25		
	interior	2.94 ± 0.10	19.5 ± 0.6	6.23 ± 0.31		
NWA 4472		10.83 ± 0.22	57.5 ± 1.7	9.74 ± 0.19		20–80
NWA 4734	0–1 mm	2.68 ± 0.09	18.1 ± 0.6	4.29 ± 0.12		330
	1–3 mm	2.77 ± 0.06	18.5 ± 0.9	4.48 ± 0.12		
	interior	2.91 ± 0.06	17.8 ± 0.6	4.66 ± 0.12		
	interior	2.79 ± 0.04	16.5 ± 0.6	4.40 ± 0.11		
NWA 4884		5.85 ± 0.09	30.7 ± 1.0	8.14 ± 0.24		180
NWA 4932		3.31 ± 0.05	27.6 ± 1.1	5.78 ± 0.29		>1100
NWA 4936		0.429 ± 0.009	1.40 ± 0.13	0.41 ± 0.03		30–80

Gd, and Er is one of the important indicators to understand the neutron energy spectra in association with the interaction of cosmic rays with planetary materials.

In this study, we effectively utilize the data set of spallogenic and neutron-captured products collected from the same fragmental samples for the characterization of lunar meteorites. It is known that most lunar meteorites have long CRE ages despite the short transition time (<1 Ma) from the Moon to the Earth because of their long residences in a shallow region on the lunar surface (Nishiizumi et al. 1996; Hidaka et al. 2017). The cosmogenic nuclides of most lunar meteorites have been produced mainly on the lunar surface. Previous studies suggest that some lunar meteorites have complicated CRE records that cannot be simply explained by single-stage irradiation on the Moon. The combination of the data set of spallogenic and neutron-captured products in lunar meteorites provides information on the transition of the shielding depth and exposure duration at each stage of the individual meteorite species having complicated CRE records on the Moon.

2. Experiments

2.1. Samples

Thirteen lunar meteorites, Dhofar 081, Dhofar 910, Dhofar 911, Northwest Africa (NWA) 482, NWA 2995, NWA 2996, NWA 3136, NWA 3163, NWA 4472, NWA 4734, NWA 4884, NWA 4932, and NWA 4936, whose abundances of several cosmogenic nuclides, such as ^{10}Be, ^{26}Al, ^{36}Cl, and ^{41}Ca, were partly reported (Nishiizumi & Caffee 2001, 2006; Nishiizumi et al. 2004, 2016), were used to collect additional new information on the CRE records from their Sm and Er isotopic compositions. Although the Sm isotopic data of 2 of the 13 meteorites, NWA 482 and NWA 2995, were already reported in our previous work (Hidaka et al. 2017), their Er isotopic data were newly measured in this study. The data of cosmogenic nuclides together with the elemental abundances of some major elements for the 11 samples are compiled in Table 1.

Five of the thirteen samples, Dhofar 081, Dhofar 910, Dhofar 911, NWA 3163 and NWA 4932, show feldspathic lithologies (Cahill et al. 2004; Korotev 2006; Korotev et al. 2009 Hudgins et al. 2011; Nagaoka et al. 2014; McLeod et al. 2016). Dhofar 081 is known to be paired with Dhofar 911 (Korotev et al. 2006). These two include fragmental highland breccias.

Among the other eight samples, NWA 2995, NWA 2996, NWA 3136, and NWA 4936 are felspathic breccias bearing basaltic components (Korotev et al. 2009; Mercer et al. 2013; Mészáros et al. 2016). These four have higher REE contents than the feldspathic materials because of the presence of the basaltic components. NWA 2995 is considered to be paired with NWA 2996 (Korotev et al. 2009). NWA 4472 is a KREEP-rich regolith breccia (Joy et al. 2011). NWA 4734 is an unbrecciated basalt that originated from low-Ti mare volcanism around 3.0 Ga ago (Chen et al. 2019; Wu & Hsu 2020). NWA 4884 is classified as a basaltic regolith breccia and originated possibly from the southern Lacus Veris within the Orientale basin and the western mare unit (Cao et al. 2019).

2.2. Chemical Treatment

Individual samples were divided into two; one for the measurements of SRLs using AMS, and the other for the determinations of Sm and Er isotopic compositions using thermal ionization mass spectrometry (TIMS) and of REE elemental abundances using inductively coupled plasma-mass spectrometry (ICP-MS).

For SLRs measurements, 30–40 mg of each powdered sample was dissolved with a HF/HNO_3 mixture and a carrier solution containing Be and Cl. After separating Cl by AgCl precipitation, Be was separated and purified by hydroxide precipitation, cation exchange, and solvent extraction with acetylacetone. Then, Al was separated from the Al–acetylacetone complex by cation exchange. Following the separation of Cl, Be, and Al, Ca was separated from the remaining solutions by anion and cation exchange. The separation methods of Be, Al, Cl, and Ca as the analytical protocols for SLRs using AMS are given in previous studies (Nishiizumi et al. 1984a, 1984b, 1997).

For TIMS and ICP-MS analyses, 30–40 mg of each powdered sample was decomposed by a mixed acid of $HF–HClO_4$. Then, the residue was redissolved in 1 ml of 1.7 M HCl. The sample solution was divided into two portions: approximately 90% of the solution was used for the

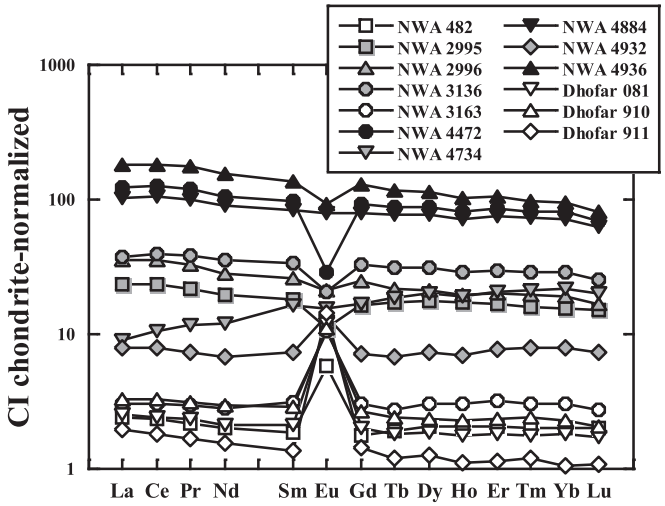

Figure 1. CI chondrite-normalized REE abundance patterns of 13 lunar meteorites used in this study.

conventional resin chemistry to separate Sm and Er for their isotopic analyses using TIMS (Triton Plus), and the other 10% of the solution was used for the determination of the elemental abundances of REEs using ICP-MS (Agilent 7500cx).

As standard reference materials for the TIMS analyses, chemical reagents of Sm and Er (1000 mg l^{-1} of single-element standard solutions for the ICP-MS and ICP-AES analyses provided by SPEX CertiPrep) were used for the determinations of their isotopic compositions.

For the chemical separation of Sm and Er, a two-step resin chemistry technique was used; the first step by cation exchange resin-packed column for the rough separation of REEs from major elements, and the second step by LN resin-packed column for mutual separation of Sm and Er from other REEs. The total procedural blank was less than 10 pg for each of Sm and Er, which is negligibly lower than the absolute amount of the element recovered from each sample through the chemical procedures. Detailed procedures of the resin chemistry were reported in our previous study (Mizutani et al. 2020).

2.3. Mass Spectrometry

Isotopic analyses of Sm and Er were performed using a TIMS machine equipped with nine Faraday cup collectors at the National Science Museum of Nature and Science, Tsukuba. All analyses were done in static mode with the amplifier rotation system. $^{147}Sm/^{152}Sm = 0.56081$ and $^{170}Er/^{166}Er = 0.44547$ were used as normalization values for the correction of instrumental mass fractionation. The analytical protocols for the conditions of the isotopic measurements of Sm and Er using TIMS, including the cup configurations, filament conditions, integration times, and so on, were described in our previous studies (Hidaka & Yoneda 2014; Mizutani et al. 2020; Hidaka et al. 2020).

AMS measurements were performed at the Lawrence Livermore Laboratory and the Purdue Rare Isotope Measurement Laboratory (PRIME Lab) at Purdue University.

3. Results

3.1. REE Characteristics

The lithological properties of individual samples can be characterized from their REE abundances, as shown in Figure 1. The feldspathic species, Dhofar 081, Dhofar 910, Dhofar 911, NWA 482, and NWA 3163, show low contents of REEs with relatively flat REE patterns and clearly positive Eu anomalies. NWA 2995, NWA 2996, NWA 3136, NWA 4734, and NWA 4932, classified as intermediate-iron lunar meteorites with low to moderate concentrations of incompatible elements (Korotev et al. 2009), show intermediate REE contents in their REE abundances in the range of 8 to 50 × CI chondrite (CI). Because NWA 4472, NWA 4884, and NWA 4936 are regolith breccias including high-REE components such as REE-rich merrillite, KREEP, or mare basalt (Jolliff et al. 1993; Korotev et al. 2009), their patterns show high REE contents over the range of 100 × CI.

3.2. Sm and Er Isotopic Compositions

Samarium has seven stable isotopes with mass numbers, 144, 147, 148, 149, 150, 152, and 154. Because ^{149}Sm has a very large thermal neutron capture cross section ($\sigma_{th} = 4.2 \times 10^4$ barn at $E = 0.0253$ eV), an isotopic shift from ^{149}Sm to ^{150}Sm caused by the neutron-capture reaction of $^{149}Sm(n,\gamma)^{150}Sm$ is expected in the presence of certain amounts of thermal neutrons arising by spallation reactions in association with the cosmic-ray irradiation. Isotopic data of Sm for the 13 lunar meteorites used in this study are listed in Table 2. Although the Sm isotopic data of NWA 482 and NWA 2995 have already been reported in our previous study (Hidaka et al. 2017), they are also shown in the table to compare with other data. All of the samples show significant variations of $^{149}Sm/^{152}Sm$ and $^{150}Sm/^{152}Sm$ in the range of $-82 < \epsilon^{149}Sm < -3.5$ and $+6.2 < \epsilon^{150}Sm < +152$, respectively. In particular, the isotopic variations of $^{149}Sm/^{152}Sm$ and $^{150}Sm/^{152}Sm$ found in NWA 4884 exceed those in any lunar surface materials recovered by the Apollo mission (Hidaka & Yoneda 2007), which correspond to a neutron fluence over 1×10^{17} neutrons cm^{-2}. Figure 2(A) is a three-isotope plot diagram of Sm to reveal the isotopic variations caused by neutron-capture reactions from the correlation between $^{149}Sm/^{152}Sm$ and $^{150}Sm/^{152}Sm$ isotopic ratios for the individual lunar meteorites used in this study. Almost all data points in the figure are plotted on the line with a slope of −1 in the figure, because the depletion of the isotopic abundance for ^{149}Sm should correspond to the enrichment of that for ^{150}Sm caused by the neutron capture reaction of $^{149}Sm(n,\gamma)^{150}Sm$. It is easily understandable that the variations are due to the isotopic shift from ^{149}Sm to ^{150}Sm caused by the neutron capture reaction of $^{149}Sm(n,\gamma)^{150}Sm$.

Erbium has six stable isotopes with mass numbers 162, 164, 166, 167, 168, and 170. Considering the RI for the neutron-capture cross section of ^{167}Er in the epithermal energy region (0.5 eV < E < 0.5 MeV), ^{167}Er can react with not only thermal neutrons but also epithermal neutrons. Then, the isotopic shift of ^{167}Er–^{168}Er caused by $^{167}Er(n,\gamma)^{168}Er$ can be used to quantify the epithermal neutron fluences (Hidaka et al. 2020). Although the neutron-capture cross section of ^{167}Er is 2 orders of magnitude smaller than that of ^{149}Sm, the isotopic variations of ^{167}Er in most samples used in this study are expected to be detectable by consideration of the neutron fluences evaluated

Table 2
Sm Isotopic Data Normalized to $^{147}Sm/^{152}$ Sm = 0.56081

	$^{144}Sm/^{152}Sm$	$^{148}Sm/^{152}Sm$	$^{149}Sm/^{152}Sm$	$^{150}Sm/^{152}Sm$	$^{154}Sm/^{152}Sm$	$\varepsilon^{149}Sm$	$\varepsilon^{150}Sm$
Dhofar 081	0.114975 ± 13	0.420499 ± 11	0.513741 ± 10	0.278939 ± 9	0.850791 ± 29	−59.90 ± 0.26	107.03 ± 0.37
Dhofar 910	0.114979 ± 15	0.420491 ± 11	0.513681 ± 9	0.279385 ± 10	0.850751 ± 33	−61.06 ± 0.25	123.20 ± 0.41
Dhofar 911	0.114972 ± 12	0.420483 ± 9	0.516619 ± 10	0.276157 ± 9	0.850786 ± 17	−4.22 ± 0.26	6.23 ± 0.37
NWA 482[a]	0.114978 ± 1	0.420439 ± 1	0.513097 ± 3	0.279392 ± 3	0.850779 ± 7	−72.36 ± 0.18	123.45 ± 0.21
NWA 2995[a]	0.114978 ± 1	0.420440 ± 1	0.513809 ± 1	0.279026 ± 1	0.850780 ± 3	−58.59 ± 0.17	110.19 ± 0.19
NWA 2996	0.114978 ± 5	0.420443 ± 7	0.513830 ± 5	0.279233 ± 4	0.850790 ± 13	−58.18 ± 0.20	117.69 ± 0.23
NWA 3136	0.114971 ± 3	0.420456 ± 3	0.514957 ± 3	0.277858 ± 2	0.850784 ± 6	−36.38 ± 0.18	67.87 ± 0.19
NWA 3163	0.114972 ± 4	0.420463 ± 4	0.516160 ± 4	0.276547 ± 4	0.850794 ± 19	−13.10 ± 0.19	20.36 ± 0.23
NWA 4472	0.114979 ± 1	0.420430 ± 1	0.516288 ± 1	0.276539 ± 1	0.850774 ± 5	−10.62 ± 0.18	20.07 ± 0.19
NWA 4734	0.114974 ± 3	0.420435 ± 2	0.514630 ± 4	0.278449 ± 3	0.850779 ± 11	−42.70 ± 0.19	89.28 ± 0.21
NWA 4884	0.114974 ± 7	0.420450 ± 6	0.512589 ± 6	0.280166 ± 5	0.850793 ± 10	−82.19 ± 0.21	151.49 ± 0.26
NWA 4932	0.114971 ± 6	0.420444 ± 4	0.516656 ± 5	0.276277 ± 4	0.850781 ± 16	−3.50 ± 0.20	10.58 ± 0.23
NWA 4936	0.114978 ± 3	0.420417 ± 3	0.516371 ± 3	0.276431 ± 2	0.850785 ± 9	−9.02 ± 0.18	16.16 ± 0.20
STD (n = 10)	0.114972 ± 2	0.420415 ± 6	0.516837 ± 9	0.275985 ± 5	0.850796 ± 15		

Notes. The number of analytical errors (2SD for individual samples and 2SE for the standard material) is given in the last digit of individual data.

The ε-notation is defined as $\varepsilon^{i}Sm = \left\{ \frac{\left(\frac{^{i}Sm}{^{152}Sm}\right)_{sample}}{\left(\frac{^{i}Sm}{^{152}Sm}\right)_{STD}} - 1 \right\} \times 10^{4}$ (i = 149, 150).

[a] The data of NWA 482 and NWA 2995 are from Hidaka et al. (2017).

from the Sm isotopic variations. Isotopic data of Er are listed in Table 3. Nine of the thirteen samples, except Dhofar 911, NWA 4472, NWA 4932, and NWA 4936, show small but significant isotopic variations of $^{167}Er/^{166}Er$ and $^{168}Er/^{166}Er$ in the range of $-4.0 < \epsilon^{167}Er < -0.4$ and $+0.8 < \epsilon^{168}Er < +4.3$, respectively. It is evident from the isotopic data points shown in Figure 2(B) as the Er three-isotope plot diagram that the isotopic variations of $^{167}Er/^{166}Er$ and $^{168}Er/^{166}Er$ are caused by the neutron-capture reaction of $^{167}Er(n,\gamma)^{168}Er$. All data points are plotted on the line with a slope of −1 in the figure, indicating that the isotopic decrements of ^{167}Er correspond to the isotopic increments of ^{168}Er resulting from the neutron-capture reaction of $^{167}Er(n,\gamma)^{168}Er$.

3.3. The Abundances of Cosmogenic Nuclides

The data of cosmogenic nuclides ^{10}Be, ^{26}Al, ^{36}Cl, and ^{41}Ca were partly reported in related meetings and conferences but have not been published yet (Nishiizumi & Caffee 2001, 2006; Nishiizumi et al. 2004, 2016; Hidaka et al. 2019). These data are compiled and listed in Table 1. The abundances of individual cosmogenic nuclides show the spread, such as 0.045 to 10.83 for ^{10}Be, 0.334 to 57.5 for ^{26}Al, 0.10 to 9.74 for ^{36}Cl, and 2.57 to 215 for ^{41}Ca, in dpm kg^{-1} unit, as shown in Table 1, because their production rates vary with the chemical composition and the depth of the target material. Although the comprehensive collection of the SRLs data provide further constraints to understand the exposure histories of the meteorites, the low ^{41}Ca activities in some samples make this difficult. The combination of the data set for cosmogenic nuclides provides information on the depth location of the meteorite species from the surface of their parent bodies (2π irradiation), and/or the preatmospheric size in space (4π irradiation) from a comparison of the measured data with the calculated data. There are two major models for the calculation of the production rates of SLRs based on the Los Alamos High Energy Transport Code System (LCS model by Masarik & Reedy 1994) and on the statistical estimation for a multielement target system (semiempirical model by Honda 1988; Nagai et al. 1993). Although the calculated data for the production rates of SLRs are somewhat model-dependent between LCS and semiempirical models (Welten et al. 2003), it is known that the measured data of SLRs for the Apollo-15 (A-15) lunar regolith core materials are in good agreement with those of calculated data by the LCS model (Nishiizumi et al. 1984a, 1984b, 1997) in the range of depth from the near surface to around 400 g cm^{-2} on the Moon. In this study, estimations of the burial depths of individual lunar meteorites on the Moon were performed from a comparison of the measured SLR data with the calculated data by the LCS model. The estimated depths for individual samples are also listed in Table 1.

4. Discussion

4.1. Exposure History of Lunar Meteorites

Because the production rates of SLRs such as ^{10}Be, ^{26}Al, ^{36}Cl, and ^{41}Ca caused by spallation and neutron-capture reactions vary along with the depth in the target materials for Galactic cosmic-ray (GCR) irradiation, the depth information of the target material can be estimated from the combination of the abundances of SLRs. It is known that most lunar meteorites have long CRE durations despite their short transition time from the Moon to the Earth (Nishiizumi et al. 1996). This suggests that most of them had experienced long CRE durations on the surface of the Moon. Because their residence durations on the surface of the Moon are considered to be generally longer than the lifetime of SLRs, their CRE ages cannot be estimated only from the SLR data. On the other hand, the ^{149}Sm–^{150}Sm isotopic shift is proportional to the CRE ages, because the neutron-capture reaction of $^{149}Sm(n,\gamma)^{150}Sm$ produces and accumulates the isotopic variations of the stable isotopes, ^{149}Sm and ^{150}Sm. The data set from a comprehensive combination between the abundances of SLRs and $^{150}Sm/^{149}Sm$ isotopic ratios in the same fragmental sample

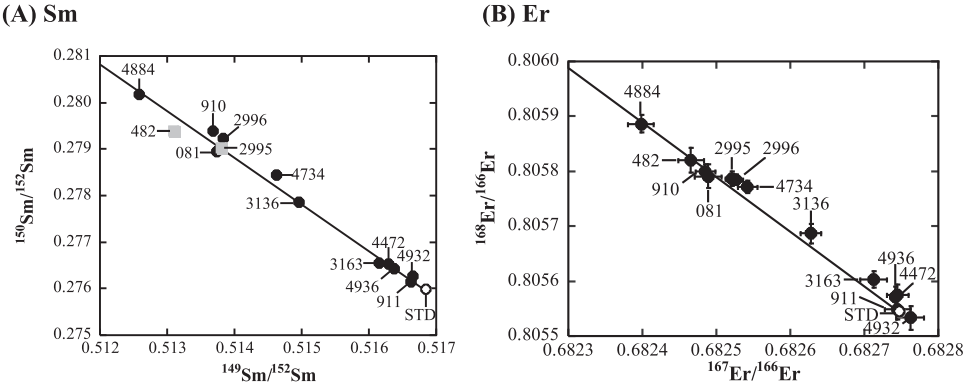

Figure 2. Correlation diagrams between (A) ^{149}Sm/^{152}Sm and ^{150}Sm/^{152}Sm, and (B) ^{167}Er/^{166}Er and ^{168}Er/^{166}Er, resulting from the neutron-capture reactions of ^{149}Sm(n,γ)^{150}Sm and ^{167}Er(n,γ)^{168}Er, respectively. The Sm isotopic data of NWA 482 and NWA 2995 in the figure are from Hidaka et al. (2017). "STD" in the figure stands for terrestrial standard materials whose isotopic data are shown in Tables 2 and 3. The solid lines in the figures show ideal neutron-capture lines showing a slope of −1.

provides useful information on the CRE situations of individual lunar meteorites that resided on the surface of the Moon.

^{150}Sm/^{149}Sm isotopic ratios of the lunar surface materials vary with the depth, simply showing the frequencies of interactions between the atoms consisting of the materials and cosmic rays that penetrated the layer. The regolith materials of a 2.4 m length drilling core collected from the A-15 landing site are the best samples to understand isotopic evidence for the depth-dependence of the interaction of cosmic rays with planetary materials, because the samples had preserved the irradiation record without stratigraphical disturbance for around 450 Ma (Russ 1972; Hidaka et al. 2000b). Because the ^{150}Sm/^{149}Sm isotopic ratios in the A-15 regolith core show a smooth curve along with the depths, they are used as a function of the depth. Then, the fitting curve prepared from the data set of the A-15 regolith core can be used as a reference to calibrate the cosmic-ray exposure duration of individual lunar meteorites buried in a regolith layer on the moon (Hidaka et al. 2017).^{150}Sm/^{149}Sm isotopic variations corresponding to neutron fluences that are proportional to the GCR exposure duration are considered to be a function of the depth for the A-15 drill core samples. The ^{150}Sm/^{149}Sm isotopic ratios are proportional to the exposure duration.

First, the model for the single-stage GCR irradiation on the Moon would be applied for the individual lunar meteorites. While being exposed by cosmic rays, the lunar meteorites are assumed to have resided at certain depths for a long time before transportation to the earth. In this case, the depth on the Moon for each meteorite can be determined from the combination of the SLR data set, as shown in Table 1. As well as the SLRs abundances, ^{150}Sm/^{149}Sm isotopic variations related to the neutron-capture reaction show a function of depth (Russ 1972; Hidaka et al. 2000b). Based on the fitting curve of the ^{150}Sm/^{149}Sm isotopic variations as a function of depth for the A-15 regolith core, the CRE duration can be determined from the adjustment of the fitting curve by extension or contraction along with the direction of ^{150}Sm/^{149}Sm isotopic ratios. Figure 3 shows a correlation diagram between ^{150}Sm/^{149}Sm isotopic ratios and depth on the Moon. All data of individual lunar meteorites are from Tables 1 – 3.

In our previous study, the data from NWA 482 and NWA 2995 are already reported, and support the single-stage irradiation model on the Moon (Hidaka et al. 2017). In this study, the data from 9 of the other 11 meteorites, Dhofar 081, Dhofar 910, NWA 2996, NWA 3136, NWA 3163, NWA 4472, NWA 4734, NWA 4884, and NWA 4936, can be explained by the single-stage irradiation model. On the assumption of the single-stage irradiation model, these nine meteorites had resided at depths from 50 to 330 g cm^{-2} for 140 to 870 Ma. On the other hand, the data from two meteorites, Dhofar 911 and NWA 4932, cannot be explained by the single-stage irradiation model. The burial depths of these two meteorites are assigned at over 1000 g cm^{-2} from the combination of the SLR abundances. However, it is unlikely to produce a significant variation of ^{150}Sm/^{149}Sm by neutron capture at the deeper level of over 1000 g cm^{-2} in the Moon even for longer than 4500 Ma, considering the depth-dependence of Sm isotopic shifts observed in the lunar regolith drill core. It is reasonable to consider a multistage, at least two-stage, irradiation model to interpret the GCR irradiation situations for Dhofar 911 and NWA 4932. We propose the model, as a simple case, that these two meteorites had once resided at a shallower depth, preserved the Sm isotopic shifts, and then migrated to a deeper level over 1000 g cm^{-2} before ejection from the Moon. In the shortest case at the first stage, the original materials for Dhofar 911 and NWA 4932 had been irradiated at a depth of 155 g cm^{-2} for 38.1 Ma and 51.4 Ma, respectively, and then moved into a deeper level above 1000 g cm^{-2} as the second stage before ejection from the Moon (see the right of Figure 3). The SLR records at the first stage disappeared because of their shorter half-life relative to the total irradiation duration but were preserved after migration to the deeper site at the second stage. On the other hand, the Sm isotopic variations had been accumulated since the first stage, although they were little affected at the second stage. In general, however, it is unlikely that the materials had migrated to a deeper level at the second stage. It is conceivable for Dhofar 911 and NWA 4932 that new regolith layers covered on the original layer after the first-stage irradiation by the gardening process and that two species apparently changed the depth to deeper levels.

4.2. Neutron Energy Spectra

Considering the numerous variations of neutron-capture cross sections along with the neutron energy, ^{167}Er reacts with both thermal and epithermal neutrons and changes its isotopic abundance by the neutron-capture reaction of ^{167}Er(n,γ)^{168}Er because of the large RI of ^{167}Er in the epithermal neutron energy region (0.5 eV $< E <$ 2000 eV). On the other hand,

Table 3
Er isotopic data normalized to $^{170}Er/^{166}Er = 0.44547$

	$^{162}Er/^{166}Er$	$^{164}Er/^{166}Er$	$^{167}Er/^{166}Er$	$^{168}Er/^{166}Er$	$\varepsilon^{167}Er$	$\varepsilon^{168}Er$
Dhofar 081	0.004049 ± 5	0.047785 ± 18	0.682489 ± 18	0.805791 ± 22	−3.65 ± 0.30	3.17 ± 0.28
Dhofar 910	0.004045 ± 4	0.047788 ± 12	0.682485 ± 13	0.805799 ± 14	−3.71 ± 0.24	3.26 ± 0.18
Dhofar 911	0.004045 ± 5	0.047788 ± 11	0.682745 ± 17	0.805548 ± 18	0.10 ± 0.29	0.15 ± 0.23
NWA 482	0.004047 ± 5	0.047785 ± 12	0.682466 ± 17	0.805820 ± 23	−3.98 ± 0.29	3.53 ± 0.29
NWA 2995	0.004047 ± 5	0.047788 ± 18	0.682521 ± 9	0.805787 ± 13	−3.18 ± 0.20	3.12 ± 0.17
NWA 2996	0.004047 ± 5	0.047789 ± 20	0.682526 ± 10	0.805785 ± 10	−3.11 ± 0.21	3.09 ± 0.13
NWA 3136	0.004049 ± 3	0.047781 ± 7	0.682628 ± 14	0.805687 ± 18	−1.61 ± 0.25	1.87 ± 0.23
NWA 3163	0.004047 ± 4	0.047789 ± 6	0.682713 ± 18	0.805603 ± 15	−0.37 ± 0.30	0.83 ± 0.19
NWA 4472	0.004048 ± 8	0.047781 ± 20	0.682745 ± 14	0.805575 ± 19	0.10 ± 0.25	0.48 ± 0.24
NWA 4734	0.004045 ± 8	0.047788 ± 19	0.682542 ± 13	0.805772 ± 11	−2.87 ± 0.24	2.93 ± 0.15
NWA 4884	0.004049 ± 5	0.047785 ± 9	0.682398 ± 18	0.805886 ± 16	−4.98 ± 0.30	4.34 ± 0.20
NWA 4932	0.004049 ± 4	0.047789 ± 17	0.682762 ± 19	0.805533 ± 22	−0.35 ± 0.31	−0.04 ± 0.28
NWA 4936	0.004047 ± 1	0.047784 ± 1	0.682742 ± 4	0.805572 ± 18	0.06 ± 0.16	0.45 ± 0.23
STD (n = 10)	0.004047 ± 1	0.047784 ± 2	0.682738 ± 10	0.805536 ± 4		

Note. The number of analytical errors (2SD for individual samples and 2SE for the standard material) is given in the last digit of individual data.

The ε-notation is defined as $\varepsilon^{i}\mathrm{Er} = \left\{ \frac{\left(\frac{^{i}\mathrm{Er}}{^{166}\mathrm{Er}}\right)_{\mathrm{sample}}}{\left(\frac{^{i}\mathrm{Er}}{^{166}\mathrm{Er}}\right)_{\mathrm{STD}}} - 1 \right\} \times 10^{4} (i = 167, \quad 168)$.

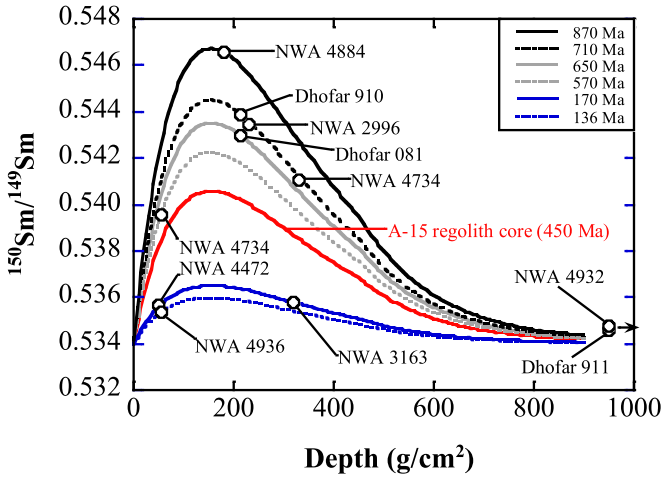

Figure 3. Fitting curves of the variation of $^{150}Sm/^{149}Sm$ isotopic ratios as a function of the depth (g cm^{-2}) on the lunar surface and the data points of 11 lunar meteorites used in this study. The depth data of all meteorites were given from the SLR data shown in Table 1. Individual fitting curves of the meteorites were prepared by expansion or contraction of the data of the fitting curve of the A-15 regolith core given by Hidaka et al. (2000). Although most data points, 9 of 11, are plotted on the fitting curves, 2 data points, for NWA 4932 and Dhofar 911, are not plotted on the curves. The result shows that 2 of 11 lunar meteorites, NWA 4932 and Dhofar, cannot be explained by the single-stage irradiation model on the Moon and that they have experienced more complicated irradiation records.

^{149}Sm sensitively reacts with thermal neutrons because of its large cross section in the thermal neutron energy region and changes its isotopic abundance by the neutron-capture reaction of $^{149}Sm(n,\gamma)^{150}Sm$. In our previous study (Hidaka et al. 2020), thermal and epithermal neutron fluences at the lunar surface were estimated from the combination of Sm and Er isotopic variations. As a result, the neutron fluences in the epithermal region are more than 10 times larger than those in the thermal region in the regolith layer at the A-15 landing site (Hidaka et al. 2020). It is known that the energy balance of thermal and epithermal neutrons arising at the lunar surface depends upon the chemical composition of the material (Lawrence et al. 2006). Since the lunar meteorites show long CRE experience on the lunar surface, they are also expected to have similar neutron energy spectra to the lunar regolith. The volume of epithermal neutron fluence is enough to affect the change in the isotopic abundance of ^{149}Sm. The capture reaction for epithermal neutrons is not negligible for the estimation of thermal and epithermal neutron fluences from Sm isotopic data. In this study, the estimation of both thermal and epithermal neutrons can be performed from the combination of $^{150}Sm/^{149}Sm$ and $^{168}Er/^{167}Er$ isotopic ratios (Hidaka et al. 2020). We simply use the following equation for the calculation of the thermal and epithermal neutron fluences from the variations of $^{150}Sm/^{149}Sm$ and $^{168}Er/^{167}Er$ isotopic ratios:

$$\sigma\Psi = \sigma_{\mathrm{th}}\Psi_{\mathrm{th}} + \sigma_{\mathrm{epi}}\Psi_{\mathrm{epi}} = \ln\left(\frac{1+R}{1+R_0}\right),$$

where σ_{th} is the cross section for thermal neutron capture, σ_{epi} is the cross section for epithermal neutron capture, Ψ_{th} is the thermal neutron fluence, Ψ_{epi} is the epithermal neutron fluence, R_0 and R are the isotopic ratios before and after neutron capture reactions ($^{150}Sm/^{149}Sm$ for Sm and $^{168}Er/^{167}Er$ for Er). In this paper, $^{150}Sm/^{149}Sm = 0.533988$ and $^{168}Er/^{167}Er = 1.17986$, resulting from the measurements of the standard reference materials, can be used as R_0.

The results of thermal and epithermal neutron fluences for individual meteorites estimated from Sm and Er isotopic ratios are listed in Table 4. The epithermal neutron fluences of 4 of the 13 meteorites used in this study, Dhofar 911, NWA 4472, NWA 4932, and NWA 4936, cannot be estimated because of their small variation in the $^{168}Er/^{167}Er$ isotopic ratios within the analytical uncertainties (see Table 3). Because the thermal neutron-capture cross section of ^{149}Sm is very large, the estimation of thermal neutron fluences from the Sm isotopic variations is possible to quantify the fluence up to 10^{14} neutrons cm^{-2}. On the other hand, the isotopic variation of ^{167}Er caused by epithermal neutrons is less sensitive than that of ^{149}Sm. The detection limit of epithermal neutron fluence is at

Table 4
The Evaluation of the Thermal (Ψ_{th}) and Epithermal Neutron Fluences (Ψ_{epi}), and the Related Information for the Individual Lunar Meteorites Used in This Study

Sample	$^{150}Sm/^{149}Sm$	$^{168}Er/^{167}Er$	Σ_{eff} (cm^2 g^{-1})	Ψ_{th} ($\times10^{16}$)	Ψ_{epi} ($\times10^{17}$)	$\Psi_{epi}\Psi_{th}$
Dhofar 081	0.542957 ± 20	1.180655 ± 45	0.0032	9.92 ± 0.03	10.05 ± 0.07	10.1 ± 0.1
Dhofar 910	0.543887 ± 21	1.180684 ± 30	0.0032	11.00 ± 0.03	10.10 ± 0.05	9.18 ± 0.05
Dhofar 911	0.534546 ± 20	1.179867 ± 40	0.0029	0.66 ± 0.03	−0.12 ± 2.93	⋯
NWA 482	0.544520 ± 7	1.180747 ± 45	0.0034	11.64 ± 0.01	10.94 ± 0.06	9.40 ± 0.05
NWA 2995	0.543053 ± 2	1.180604 ± 25	0.0054	9.87 ± 0.03	9.13 ± 0.04	9.25 ± 0.05
NWA 2996	0.543435 ± 10	1.180592 ± 23	0.0054	10.32 ± 0.04	8.86 ± 0.04	8.58 ± 0.05
NWA 3136	0.539576 ± 5	1.180272 ± 36	0.0068	6.17 ± 0.01	4.88 ± 0.11	7.91 ± 0.18
NWA 3163	0.535778 ± 8	1.180002 ± 38	0.0036	1.98 ± 0.01	1.67 ± 0.34	8.44 ± 1.72
NWA 4472	0.535630 ± 2	1.179906 ± 37	0.0081	1.89 ± 0.01	0.22 ± 1.23	⋯
NWA 4734	0.541067 ± 7	1.180546 ± 28	0.0081	7.71 ± 0.01	8.71 ± 0.05	11.3 ± 0.1
NWA 4884	0.546571 ± 12	1.180962 ± 39	0.0083	13.79 ± 0.01	13.74 ± 0.05	9.96 ± 0.04
NWA 4932	0.534740 ± 8	1.179815 ± 46	0.0043	0.90 ± 0.01	−0.95 ± 1.11	⋯
NWA 4936	0.535335 ± 6	1.179907 ± 27	0.0093	1.57 ± 0.01	0.30 ± 1.43	⋯

Note. $^{150}Sm/^{149}Sm$ and $^{168}Er/^{167}Er$ are calculated from the isotopic data in Tables 2 and 3.
The effective macroscopic cross section, Σ_{eff}, is estimated from the elemental abundances mainly of Si, Al, Fe, Ca, Mg, Ti, Sm, Eu, and Gd based on the estimation given by Lingenfelter et al. (1972).

most 10^{17} neutrons cm^{-2} roughly estimated from the analytical precisions of $^{168}Er/^{167}Er$ isotopic ratios in this study.

It is known that the energy spectrum of neutrons caused by GCR irradiation largely depends on the chemical composition of the target materials (Lingenfelter et al. 1972; Spergel et al. 1986). The bulk of target material is often treated as an effective macroscopic cross section (Σ_{eff}) evaluated from the elemental abundances of Si, Al, Fe, Ca, Mg, and Ti as major elements and Sm, Eu, and Gd as minor elements in the individual materials (Lingenfelter et al. 1972). Figure 4 shows a correlation diagram between the variation of neutron fluence ratio Ψ_{epi}/Ψ_{th} and the macroscopic cross section Σ_{eff} for individual meteorites. The variations of Ψ_{epi}/Ψ_{th} depending on Σ_{eff} are unclear for the data of the lunar meteorites. For comparison of the data between the meteorites and the A-15 regolith samples, all of the data points are plotted in the same figure. The data set in Figure 4 seems to have a trend in which larger Σ_{eff} result in larger energy balance between thermal and epithermal neutrons, considering that the A-15 regolith samples have higher $\epsilon_{Er}/\epsilon_{Sm}$ and Σ_{eff} relative to the meteorites.

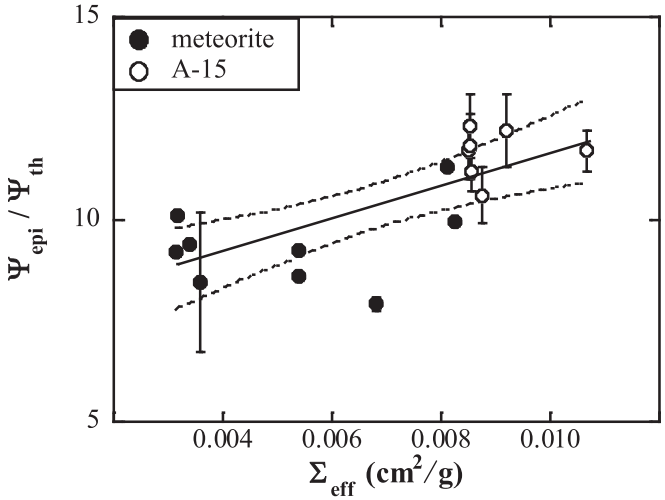

Figure 4. A diagram for the energy balance between thermal and epithermal neutrons (Ψ_{epi}/Ψ_{th}) and the effective macroscopic neutron-capture cross sections (Σ_{eff}) for lunar meteorites. For comparison, the data points from A-15 samples are also plotted in the same figure. The solid line in the figure reveals a regression line with a correlation coefficient of $r = 0.73$. The broken lines in the figures show 95% confident intervals.

5. Conclusions

The data set of cosmogenic nuclides as spallation and neutron-captured products for the 13 lunar meteorites could be effectively utilized for the estimation of the original depth from the lunar surface and CRE duration on the Moon on the assumption of a single-stage irradiation model. In this study, the Sm and Er isotopic variations caused by the neutron-capture reactions of $^{149}Sm(n,\gamma)^{150}Sm$ and $^{167}Er(n,\gamma)^{168}Er$, respectively, were newly found in most lunar meteorites. As a new attempt to discuss the energy distribution of neutrons induced from cosmic-ray irradiation, a combination of the isotopic shifts of ^{149}Sm–^{150}Sm and ^{167}Er–^{168}Er was applied for the determination of the neutron fluences of thermal and epithermal energy ranges. The results of the balance between the thermal and epithermal neutron fluences of nine lunar meteorites are reasonably comparable with those of the regolith materials collected from the lunar surface within the depth of 412 g cm^{-2}. This also supports the previous result on the CRE conditions of most lunar meteorites having a long residence time (140–870 Ma) near the surface of the Moon and the short transition time (<1 Ma) from the Moon to the Earth.

ORCID iDs

Hiroshi Hidaka https://orcid.org/0000-0001-7239-4086
Shigekazu Yoneda https://orcid.org/0000-0003-2306-4261

References

Cahill, J. T., Floss, C., Anand, M., et al. 2004, M&PS, 39, 503
Cao, H., Chen, J., Fu, X., & Ling, Z. 2019, JRSp, 51, 1652
Chen, J., Jolliff, B. L., Wang, A., et al. 2019, JGRE, 124, 2583
Hidaka, H., Ebihara, M., & Yoneda, S. 1999, E&PSL, 173, 41
Hidaka, H., Ebihara, M., & Yoneda, S. 2000a, E&PSL, 180, 29
Hidaka, H., Ebihara, M., & Yoneda, S. 2000b, M&PS, 35, 581
Hidaka, H., Mizutani, Y., & Yoneda, S. 2020, ApJ, 904, 183
Hidaka, H., Nishiiuzmi, K., Caffee, M., & Yoneda, S. 2019, M&PS, 54, A157
Hidaka, H., Sakuma, K., Nishiizumi, K., & Yoneda, S. 2017, AJ, 815, 76
Hidaka, H., & Yoneda, S. 2007, GeCoA, 71, 1074
Hidaka, H., & Yoneda, S. 2014, ApJ, 786, 138
Honda, M. 1988, Metic, 23, 3
Honda, M., Caffee, M. W., Miura, Y. N., Nagai, H., & Nishiizumi, K. 2002, M&PS, 37, 1711

Hudgins, J. A., Kelley, S. P., Korotev, R. L., & Spray, J. G. 2011, GeCoA, 75, 2865
Imamura, M., Finkel, R. C., & Wahlen, M. 1973, E&PSL, 20, 107
Jolliff, B. L., Haskin, L. A., Colson, R. O., & Wadhwa, M. 1993, GeCoA, 57, 4069
Joy, K. H., Burgess, R., Hinton, R., et al. 2011, GeCoA, 75, 2420
Korotev, R. L. 2006, LPSC, 37, 1404
Korotev, R. L., Zeigler, R. A., & Jolliff, B. L. 2006, GeCoA, 70, 5935
Korotev, R. L., Zeigler, R. A., Jolliff, B. L., Irving, A. J., & Bunch, T. E. 2009, M&PS, 44, 1287
Lawrence, D. J., Feldman, W. C., Elphic, R. C., et al. 2006, JGR, 111, E08001
Lingenfelter, R. E., Canfield, E. H., & Hampel, V. E. 1972, E&PSL, 16, 355
Masarik, J., & Reedy, R. 1994, GeCOA, 58, 5307
McLeod, C. L., Brandon, A. D., Fernandes, V. A., et al. 2016, GeCoA, 187, 350
Mercer, C. N., Treiman, A. H., & Joy, K. H. 2013, M&PS, 48, 289
Mészáros, M., Hofman, B. A., Lanai, P., et al. 2016, M&PS, 51, 1830
Mizutani, Y., Hidaka, H., & Yoneda, S. 2020, Geochem. J., 54, 381
Nagai, H., Honda, M., Imamura, M., & Kobayashi, K. 1993, GeCoA, 57, 3705
Nagaoka, H., Takeda, H., Karouji, Y., et al. 2014, EPS, 66, 115
Nishiizumi, K., & Caffee, M. W. 2001, LPSC, 32, 2101
Nishiizumi, K., & Caffee, M. W. 2006, M&PS, 41, A133
Nishiizumi, K., Caffee, M. W., & Jull, A. J. T. 2016, M&PS, 51, A487
Nishiizumi, K., Caffee, M. W., Jull, A. J. T., & Reedy, R. C. 1996, M&PS, 31, 893
Nishiizumi, K., Elmore, D., Ma, X. Z., & Arnold, J. R. 1984a, E&PSL, 70, 157
Nishiizumi, K., Fink, D., Klein, J., Middleton, R., Masarik, J., & Reedy, R. C. 1997, E&PSL, 148, 545
Nishiizumi, K., Hillegonds, D. J., McHargue, L. R., & Jull, A. J. T. 2004, LPSC, 35, 1130
Nishiizumi, K., Klein, J., Middleton, R., & Arnold, J. R. 1984b, E&PSL, 70, 164
Russ, G. P., Burnett, D. S., Wasserburg, G. J., et al. 1972, E&PSL, 15, 172
Spergel, M. S., Reedy, R. C., Lazareth, O. W., Levy, P. W., & Slatest, L. A. 1986, JGR, 91, D483
Welten, K. C., Caffee, M. W., Hillegonds, D. J., et al. 2011, M&PS, 46, 177
Welten, K. C., Caffee, M. W., Leya, I., et al. 2003, M&PS, 38, 157
Wu, Y., & Hsu, W. 2020, Icar, 338, 113531